Changing-look behaviour and amplitude-modulated QPO in blazar Ton 599

Guohai Chen,[1,2,3] Wenxin Yang,[1,2,3] Yi Liu,[1,2,3]★ Luis C. Ho,[4,5] Hubing Xiao,[6] Rumen S. Bachev,[7] Anton Strigachev[7] and Junhui Fan[1,2,3]★

[1]*Center for Astrophysics, Guangzhou University, Guangzhou 510006, China*
[2]*Greater Bay Brand Center of the National Astronomical Data Center, Guangzhou 510006, China*
[3]*Astronomy Science and Technology Research Laboratory of Department of Education of Guangdong Province, China*
[4]*Kavli Institute for Astronomy and Astrophysics, Peking University, Beijing 100871, China*
[5]*Department of Astronomy, School of Physics, Peking University, Beijing 100871, China*
[6]*Key Lab for Astrophysics, Shanghai Normal University, Shanghai 200234, China*
[7]*Institute of Astronomy and NAO, Bulgarian Academy of Sciences, 72 Tsarigradsko Shose Blvd, 1784 Sofia, Bulgaria*

ABSTRACT

Active galactic nuclei (AGNs) are powered by supermassive black holes and exhibit different observational types, primarily due to orientation effects according to the unified model of AGN. Changing-look AGNs (CL AGNs), however, challenge this paradigm by transitioning between different types over time. A hallmark of CL AGNs is the variability of the broad emission line (BEL) flux relative to the continuum. In this study, we investigate the optical spectral evolution of Ton 599 and its correlation with the γ-ray flux in the GeV band. The optical continuum flux density exhibits strong variability, with a normalized excess variance of $F_{\mathrm{var}} = 1.089$. In contrast, the MgII flux varies with a much smaller amplitude ($F_{\mathrm{var}} = 0.194$), while the equivalent width of Mg II shows intermediate variability ($F_{\mathrm{var}} = 0.686$). A strong correlation is observed between the optical continuum and the γ-ray flux, suggesting a common origin. In addition, an amplitude-modulated quasi-periodic oscillation (QPO) with a period of ~176 d is identified in the γ-ray light curve during MJD 57000–58400, with modulation on a ~400-d time-scale. A similar QPO with a period of ~181 d is also detected in the optical g-band light curve during MJD 59500–60100. The presence of these QPOs in both bands likely reflect the influence of geometrical structures in the jet as well as long-term bursts. Our results suggest that jet dynamics may drive CL events in some AGNs, contributing to our understanding of the physical processes governing AGN jets and offering critical refinements to the unified model.

Key words: galaxies: active – quasars: general – gamma-rays: general.

1 INTRODUCTION

Most massive galaxies host supermassive black holes (SMBHs) at their centres (J. Kormendy & L. C. Ho 2013), which drive powerful emissions as they accrete surrounding material. This accretion process forms a dense and luminous region known as the active galactic nucleus (AGN). According to the unified model, the observed properties of AGNs vary with the orientation of the system relative to the observer's line of sight (P. Padovani et al. 2017). About 10 per cent of AGNs have relativistic jets that are launched from the immediate vicinity of the SMBHs (C. M. Urry & P. Padovani 1995). Blazars, a subclass of AGNs, are characterized by their relativistic jets pointing toward Earth, resulting in the relativistic (Doppler) beaming effect (R. D. Blandford & A. König 1979). This beaming causes rapid, high-amplitude variability across the electromagnetic spectrum on time-scales ranging from hours to years (J.-H. Fan et al. 2005). Blazars are classified into two subclasses based on the

equivalent width (EW) of their optical emission lines. BL Lacertae objects (BL Lacs) have an EW of less than 5 Å, while flat spectrum radio quasars (FSRQs) have an EW of 5 Å or greater (M. Stickel et al. 1991).

A striking feature of some AGNs is their ability to move from one class to another, a phenomenon known as changing-look (CL) behaviour. This challenges the paradigm of the unified model of AGNs, as it involves the appearance (turn-on, with larger EWs) or disappearance (turn-off, with weaker EWs) of optical broad emission lines (BELs) over time-scales of months to years (C. Ricci & B. Trakhtenbrot 2023). Long-term monitoring has shown that a subset of CL AGNs undergo multiple spectral transitions. For example, Mrk 1018 showed a dramatic increase in the intensity of the H β line by a factor of 6.6 in less than five years, followed by its disappearance nearly 30 yr later (R. D. Cohen et al. 1986; R. E. McElroy et al. 2016). Similarly, in Mrk 590 the H β emission line turned on in 1989 and turned off again in 2003 (K. D. Denney et al. 2014). In 2017, its broad optical emission lines reappeared, accompanied by significant continuum flux variability (S. I. Raimundo et al. 2019; A. K. Mandal et al. 2021). More recently, B. Palit et al.

★ E-mail: pinux@gzhu.edu.cn (YL); fjh@gzhu.edu.cn (JF)

(2025) showed that Mrk 590 is transitioning back to a Seyfert-1.2 state, resembling its classification in the 1990s. These transitions challenge our understanding of the physical mechanisms that drive AGN variability and spectral evolution. Similar behaviour has also been reported in blazars (e.g. J. J. Ruan et al. 2014; N. Alvarez Crespo et al. 2016; L. Foschini et al. 2021; H. D. Mishra et al. 2021; H. A. Pena-Herazo et al. 2021; K. Chand & Gopal-Krishna 2025; S.-J. Kang et al. 2025). CL blazars exhibit clear transitions between the standard FSRQs and BL Lacs, often reflected in variations of the EW of broad emission lines. These phenomena are important for understanding the origin of CL blazars and the physical drivers behind the distinction between the two subclasses, which may involve intrinsic jet variability and radiation processes (P. Giommi et al. 2012; H. D. Mishra et al. 2021), as well as changes in the accretion rate (M. Elitzur 2012; S. Boula, D. Kazanas & A. Mastichiadis 2019). Another possible explanation lies in the relative contribution of beamed jet emission compared to the unbeamed component: BL Lacs tend to have a larger intrinsic jet-to-unbeamed luminosity ratio than FSRQs, leading to weaker observed emission lines (J. H. Fan 2003).

The variability of blazars is particularly violent, usually exhibiting irregular noise-like behaviour. Studying this variability provides insights into the structure, physical properties, and radiation processes of relativistic jets (M.-H. Ulrich, L. Maraschi & C. M. Urry 1997). One especially intriguing phenomenon revealed in such studies is the quasi-periodic oscillation (QPO). QPOs are often regarded as a possible indicator of a binary supermassive black hole system, exemplified by the well-known case of OJ 287 (A. Sillanpaa et al. 1988; M. Valtonen & H. Karttunen 2006; M. J. Valtonen et al. 2008). They have also been linked to processes near the innermost stable orbit of a black hole or to oscillatory modes within the surrounding accretion disc (M. Gierliński et al. 2008; P. Lachowicz et al. 2009). Consequently, extensive searches for QPOs in blazars have been conducted at different wavelengths (e.g. C. M. Raiteri et al. 2001; J. H. Fan et al. 2002, 2007; D. Lin et al. 2013; M. Ackermann et al. 2015; A. Sandrinelli, S. Covino & A. Treves 2016b; G. Bhatta 2017; J. Zhang et al. 2017; P. Zhang et al. 2017; P.-f. Zhang et al. 2017a, 2018; G. Bhatta & N. Dhital 2020; P. Kushwaha et al. 2020; G.-W. Ren et al. 2021a, b; X.-P. Li et al. 2023; J. Chen et al. 2024; C. Levy, H. Sol & J. Bolmont 2024; P. Peñil et al. 2025). At γ-rays, the *Fermi* Gamma-ray Large Area Telescope (*Fermi*-LAT[1]; A. A. Abdo et al. 2010) has provided a powerful tool for monitoring blazars. Since M. Ackermann et al. (2015) identified PG 1553+113 as the first possible quasi-periodic GeV γ-ray blazar, supported by correlated variations in the optical and radio bands, numerous γ-ray QPOs have subsequently been reported in different blazars (e.g. A. Sandrinelli et al. 2016a, 2016b, 2018; P.-F. Zhang et al. 2017; P.-f. Zhang et al. 2017b; J. Zhou et al. 2018; A. C. Gupta et al. 2019; A. Sarkar et al. 2020, 2021; A. Roy et al. 2022; P. Peñil et al. 2025). In recent years, systematic searches for QPOs have been carried out using large samples of blazars with long-term *Fermi*-LAT data. For example, J. Chen et al. (2022) investigated 1525 highly variable γ-ray sources from the *Fermi*-LAT light curve repository and identified a 31.3-d transient QPO in S5 0716+714. Later, J. Chen et al. (2024) conducted a further systematic search for transient QPO signals in 134 bright *Fermi* blazars, identifying four new transient QPO events, including repetitive QPOs in PKS 0537–441 and nested QPOs in PKS 1424–41. H. X. Ren, M. Cerruti & N. Sahakyan (2023) analysed the light curves of the 35 brightest LAT-detected AGNs over more than a decade of observations (2008–2021), aiming to identify statistically

significant QPOs. In addition, P. Penil et al. (2025) performed a search for periodicity in 24 γ-ray blazars using twelve years of *Fermi*-LAT data, finding a weak significance of $\sim 1.8\sigma$ in PG 1553+113.

In this work, we use long-term optical spectroscopic observations from the Steward Observatory (SO[2]; P. S. Smith et al. 2009) and find that Ton 599 has undergone several optical spectral emission line transitions between 2011 January and 2018 July, including the turn-on and turn-off of its BELs. Using *Fermi*-LAT γ-ray data, we identify a QPO with a period of 176 d during MJD 57000–58400. Subsequently, a similar QPO with a period of 181 d during MJD 59500–60100 is detected in the optical g-band from the Zwicky Transient Facility (ZTF[3]; E. C. Bellm et al. 2019; F. J. Masci et al. 2019). In particular, changes in the optical spectrum are found to be strongly correlated with γ-ray flux variability. These observed behaviour can be explained by a curved jet whose orientation changes with time (M. Lainela et al. 1999; P. Mohan & A. Mangalam 2015; E. Sobacchi, M. C. Sormani & A. Stamerra 2017; J. Zhou et al. 2018; A. Sarkar et al. 2020; A. Roy et al. 2022). Magnetohydrodynamic instabilities (A. Mignone et al. 2010) or jet rotation (M. Villata & C. M. Raiteri 1999) can change the orientation of the jet, leading to variations in the Doppler factor (C. M. Raiteri et al. 2017). At small viewing angles, the beaming effect enhances the continuum emission and masks the BELs; at larger viewing angles, the BELs become visible again.

In this paper, we provide a detailed description of the Ton 599 spectral data, *Fermi* LAT data, and the analysis methods in Section 2. By combining the low-energy and high-energy bands, we conduct an in-depth investigation of the CL events and variability of Ton 599 in this section. The possible causes and implications of these findings are discussed in Section 3, and a summary is presented in Section 4. We assume a flat universe with $h = \Omega_\Lambda = 0.7$ throughout the paper.

2 DATA ANALYSIS AND RESULTS

2.1 Source of optical spectra

Ton 599 is typically classified as a FSRQ with a redshift of $z = 0.725$. It is located at Equatorial (J2000) coordinates: RA = $11^h59^m31.8339^s$, Dec. = $+29°14'43.827''$. The optical spectra analysed in this paper were obtained from publicly available data provided by the SO, University of Arizona, as part of the *Ground-based Observational Support of the Fermi Gamma-ray Space Telescope* program (P. S. Smith et al. 2009). Observations were made with the 2.3 m Bok and 1.54 m Kuiper telescopes. Between 2008 October and 2018 July, spanning ten cycles of the *Fermi* mission, 249 spectra of Ton 599 were collected. For this analysis, 191 spectra with V-band magnitude calibration were selected. The original spectra, uncorrected for Galactic dust reddening and extinction, cover a wavelength range of 4000–7550 Å with a dispersion of 4 Å pixel^{-1}. The spectral resolution, determined by the slit width used during the observations, typically ranged from 16 to 24 Å. Atmospheric absorption features, including the O_2 B-band absorption around 6980 Å and, occasionally, H_2O absorption between 7200–7300 Å during humid nights, are evident in the spectra. In addition, fringing artefacts caused by the thinned CCD are present in most spectra at wavelengths longer than 7000 Å. Given the redshift of Ton 599, we excluded rest-frame wavelengths longer than 3900 Å in our spectral analysis and visual presentation, in order to avoid contamination

---

[1] https://fermi.gsfc.nasa.gov/ssc/data/access/

[2] https://james.as.arizona.edu/~psmith/Fermi/
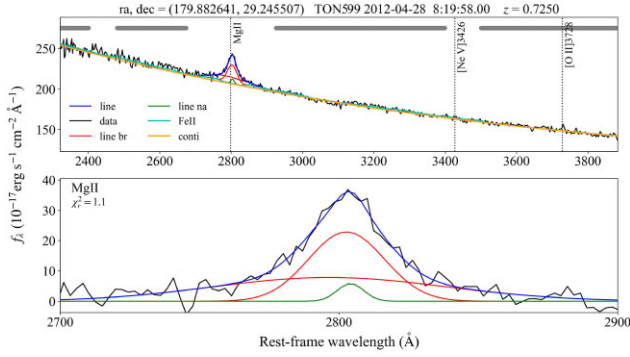[3] https://irsa.ipac.caltech.edu/Missions/ztf.html

Figure 1. The optical spectrum of Ton 599, observed on 2012 April 28, is modelled using QSOFITMORE. The black line represents the observed spectral data. Broad and narrow components of the emission lines are shown in red and green, respectively, while the fitted continuum is indicated by the orange line. The blue curve corresponds to the total modelled spectrum. Grey dashed marks at the top indicate the wavelength regions free of strong lines, which are used to fit the continuum. The spectral data are obtained from the Steward Observatory.

from strong telluric absorption and fringing artefacts (e.g. L. C. Ho, A. V. Filippenko & W. L. W. Sargent 1993).

2.2 Analysis of steward observatory optical spectra

We analysed the 191 spectra of Ton 599 using the publicly available software QSOFITMORE (Y. Fu 2021), which extracts BELs and continuum features (J.-J. Jin et al. 2023; G. Chen et al. 2024; Q. Dong et al. 2025). For completeness, we briefly describe the full spectral fitting procedure implemented in this tool. Although some components (such as host galaxy subtraction) may not be relevant for Ton 599 due to its high redshift and blazar nature, the software is designed to automatically assess their applicability and include or omit them accordingly.

This tool uses spectral models, Fe II templates, and fitting functions, and uses a reduced chi-square (χ^2) test for optimization. An example of the fitting result is presented in the Fig. 1. As a first step, the original spectra were corrected for Galactic dust reddening and extinction using the extinction curves from J. A. Cardelli, G. C. Clayton & J. S. Mathis (1989) and the dust map from D. J. Schlegel, D. P. Finkbeiner & M. Davis (1998). To minimize contamination from the host galaxy, its contribution was subtracted from the target spectra using the principal component analysis (PCA) technique described in C. W. Yip et al. (2004a, b). For efficient continuum fitting

over the entire spectrum, we modelled three components: a power law, a third-order polynomial (used to fit complex continuum shapes), and Fe II emission templates for the optical and UV regions (T. A. Boroson & R. F. Green 1992; M. Vestergaard & B. J. Wilkes 2001). After the continuum fit, the emission line properties were determined by subtracting the best-fitting continuum from the observed spectra. The Mg II emission line, spanning the wavelength range 2700–2900 Å, was modelled with two Gaussian components for the broad emission and one Gaussian component for the narrow emission (Y. Shen et al. 2019). From this process, we extracted the flux and EW of the Mg II line, as well as the continuum flux density at 3000 Å. The detailed results are presented in Table 1.

We found that the EW of the MgII BELs of Ton 599 undergoes significant transitions over time, indicative of CL events. The Fig. 2(a) shows the temporal evolution of the EW, with 57 spectra (29.84 per cent) showing BL Lacs characteristics (EW < 5 Å) and 134 spectra (70.16 per cent) showing typical FSRQ characteristics (EW > 5 Å). Fig. 2(b) presents eleven representative spectra marked with stars in Fig. 2(a), highlighting the correlation between variations in the continuum and the emission lines transitions. In the Fig. 2(b), the main spectra on the left clearly displayed turn-off (orange) and turn-on (blue) events for the Mg II line. Each of these main spectra is also shown in a smaller box on the right, where both the vertical and horizontal axes are kept fixed to facilitate comparison of continuum levels. The baseline for flux visualization is set at $\log(\lambda f_\lambda) = -12$ (erg s^{-1} cm^{-2}), with the area between the baseline and each spectrum filled in with the corresponding colour. In the 'on' state, the continuum flux density is relatively low. Conversely, in the 'off' state, the continuum flux density is significantly enhanced. It is important to emphasize that Fig. 2 highlights frequent changes in the optical spectral emission line of Ton 599. However, these variations should not be misinterpreted as periodic; rather, they reflect the inherently non-uniform and dynamic nature of the source's spectral behaviour.

We converted the continuum flux density at 3000 Å and the Mg II line flux into luminosities using $L_\lambda = 4\pi d_L^2 \lambda F(\lambda)$, where $\lambda F(\lambda)$ is the flux density in units of erg cm^{-2} s^{-1}, $d_L = (1 + z)\frac{c}{H_0}\int_1^{1+z}\frac{1}{\sqrt{\Omega_M x^3 + 1 - \Omega_M}}dx$ is luminosity distance (D. W. Hogg 1999). The resulting luminosities are listed in Table 1. Here, we adopt the luminosity at 3000 Å to represent the continuum luminosity. Fig. 3 shows the relations between the logarithmic quantities: continuum luminosity at 3000 Å ($\log L_{3000}$), Mg II line luminosity ($\log L_{MgII}$), and Mg II equivalent width ($\log EW_{MgII}$). With increasing continuum luminosity, the EW$_{MgII}$ decreases significantly, a behaviour characteristic of the Baldwin effect (BEff; J. A. Baldwin 1977).

Table 1. The QSOFITMORE fitting results of 191 optical spectra of Ton 599. (This table is available in its entirety in machine-readable form.).

MJD day (1)	f_{3000} 10^{-17} erg s^{-1} cm^{-2} Å^{-1} (2)	f_{MgII} 10^{-17} erg s^{-1} cm^{-2} (3)	EW$_{MgII}$ Å (4)	$\log L_{3000}$ erg s^{-1} (5)	$\log L_{MgII}$ erg s^{-1} (6)
55565	68.32 ± 0.10	1273.52 ± 87.35	18 ± 1.24	45.68	43.48 ± 0.03
55594	70.88 ± 0.08	1536.89 ± 54.22	20.66 ± 0.73	45.70	43.56 ± 0.02
55597	75.06 ± 0.12	1549.63 ± 19.26	19.56 ± 0.24	45.72	43.56 ± 0.01
55599	86.78 ± 0.14	1674.4 ± 14.88	18.4 ± 0.16	45.79	43.60 ± 0
55624	75.50 ± 0.10	1618.42 ± 64.95	20.24 ± 0.81	45.73	43.58 ± 0.02
...	...	...	...	...	...

Notes. Col. (1) gives the MJD of the spectroscopic observations. Col. (2) lists the continuum flux density at 3000 Å (f_{3000}) in units of 10^{-17} erg s^{-1} cm^{-2} Å^{-1}. Col. (3) shows the MgII line flux (f_{MgII}) in units of 10^{-17} erg s^{-1} cm^{-2}. Col. (4) presents the Mg II EW (EW$_{MgII}$). Col. (5) lists the continuum luminosity at 3000 Å ($\log L3000$) in units of erg s^{-1}. Col. (6) gives the MgII line luminosity ($\log L_{MgII}$) in units of erg s^{-1}.
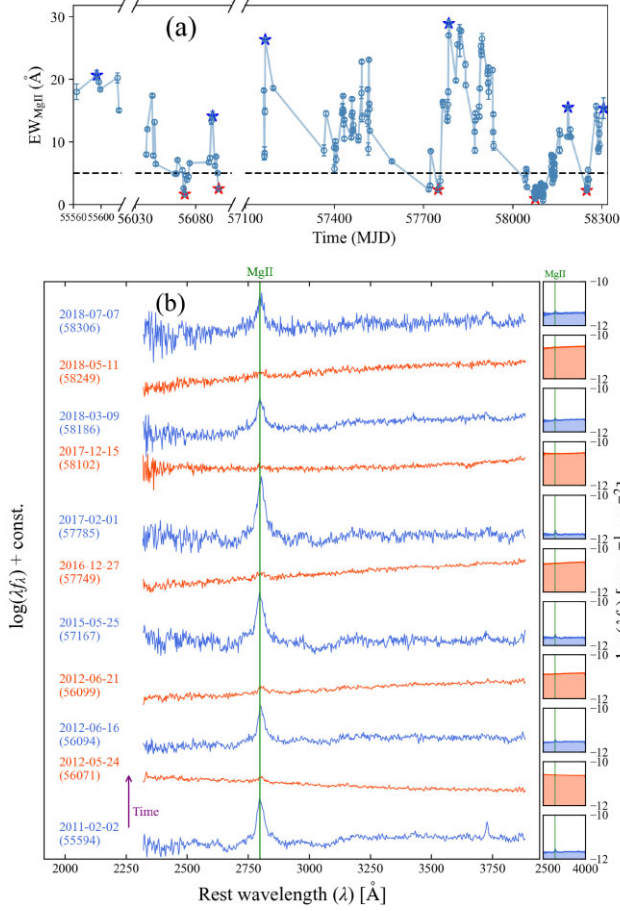
Figure 2. Top (a): The top panel displays the evolution of the Mg II EW over time, based on 191 spectra of Ton 599. The blue and red stars indicate the specific epochs corresponding to the optical spectra shown in the bottom panel. Bottom (b): The bottom panel presents a sequence of optical spectra from Ton 599, corresponding to the epochs marked with stars in the top panel. The main spectra on the left clearly displayed turn-off (orange) and turn-on (blue) events for the Mg II line. Each of these main spectra is also shown in a smaller box on the right, where both the vertical and horizontal axes are kept fixed to facilitate comparison of continuum levels. The baseline for flux visualization is set at $\log(\lambda f_\lambda) = -12$ (erg s^{-1} cm^{-2}), with the area between the baseline and each spectrum filled in with the corresponding colour.

Expressing the relation in terms of luminosities allows a direct comparison of the slope with previous studies (see Section 3.3 for details). The best-fitting relation between $\log L_{3000}$ and $\log \mathrm{EW}_{\mathrm{MgII}}$ is $\log \mathrm{EW}_{\mathrm{MgII}} = (-0.92 \pm 0.02) \log L_{3000} + (43.37 \pm 0.84)$, with a Pearson correlation coefficient of $r = -0.97$, $p < 10^{-6}$. In contrast, $\log L_{\mathrm{MgII}}$ shows no significant dependence on $\log \mathrm{EW}_{\mathrm{MgII}}$ ($r = -0.05$, $p = 0.46$), indicating that the variability of $\mathrm{EW}_{\mathrm{MgII}}$ is primarily driven by changes in the continuum rather than the line luminosity.

To quantify the intrinsic variability, we calculated the fractional variability amplitude F_{var} following R. Edelson et al. (2002):

$$F_{\mathrm{var}} = \sqrt{\frac{S^2 - \langle \sigma_{\mathrm{err}}^2 \rangle}{\langle f^2 \rangle}}, \tag{1}$$

with the corresponding uncertainty,

$$\sigma_{F_{\mathrm{var}}} = \frac{1}{F_{\mathrm{var}}} \sqrt{\frac{1}{2N}} \frac{S^2}{\langle f^2 \rangle}, \tag{2}$$
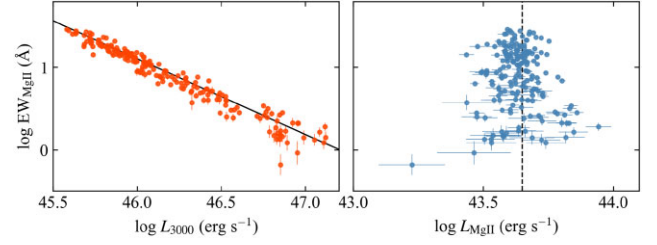

Figure 3. Correlations between the logarithmic quantities: continuum luminosity at 3000 Å ($\log L_{3000}$), Mg II line luminosity ($\log L_{\mathrm{MgII}}$), and Mg II equivalent width ($\log \mathrm{EW}_{\mathrm{MgII}}$). Left panel: $\log \mathrm{EW}_{\mathrm{MgII}}$ versus $\log L_{3000}$ shows a strong anticorrelation, with the best-fitting relation $\log \mathrm{EW}_{\mathrm{MgII}} = (-0.92 \pm 0.02) \log L_{3000} + (43.37 \pm 0.84)$ ($r = -0.97$, $p < 10^{-6}$). Right panel: $\log \mathrm{EW}_{\mathrm{MgII}}$ versus $\log L_{\mathrm{MgII}}$ shows no significant correlation ($r = -0.05$, $p = 0.46$). The vertical dashed line marks $\log L_{\mathrm{MgII}} = 43.65$ erg s^{-1}.

where S^2 is the sample variance, $\langle \sigma_{\mathrm{err}}^2 \rangle$ is the mean squared uncertainty, and $\langle f^2 \rangle$ is the mean flux squared. We obtained $F_{\mathrm{var}} = 1.089 \pm 0.056$ for f_{3000}, 0.686 ± 0.035 for $\mathrm{EW}_{\mathrm{MgII}}$, and 0.194 ± 0.055 for f_{MgII}. These results indicate that the continuum flux density exhibits the strongest variability, while the Mg II flux is much weaker.

Ton 599 exhibits multiple spectral transitions between Modified Julian Day (MJD) 55 565 (2011 January 4) and MJD 58 306 (2018 July 7), suggesting the potential presence of an underlying periodicity. However, the SO spectral observations of Ton 599 are temporally sparse, with relatively dense coverage occurring only between MJD 57 000 and MJD 58400. Even within this interval, the observation density is insufficient for a robust independent period analysis. Fortunately, the optical and γ-ray flux variations in Ton 599 are strongly correlated (I. Liodakis et al. 2018, 2019), with a near-zero time lag reported in some studies (T. Jaeger et al. 2023). For example, R. Prince (2019) identified a time lag of a few days between the optical and γ-ray flux variations from October to December 2017. Similarly, B. Rajput et al. (2024) reported a strong correlation in flux variations during MJD 58 007 to MJD 58107, which falls within the timeframe considered in this work. Despite the limitations in optical data coverage, the strong correlation between optical and γ-ray fluxes, along with periodic patterns observed in the γ-ray light curve, provides an opportunity to infer corresponding trends in the optical band.

2.3 *Fermi* LAT data analysis

We have analysed *Fermi* LAT data (P8R3_SOURCE_V3) collected between MJD 57 000 (2014 December 8) and MJD 58 300 (2018 April 16) over the energy range of 0.1–100 GeV. The analysis was performed using the FERMITOOLS software (version 2.0.8) and the associated Fermitools-data package (version 0.18). During data processing, we applied standard filtering criteria to the photon data. Specifically, a zenith angle cutoff of $< 90°$ was imposed to exclude Earth limb contamination, and only data satisfying DATA_QUAL>0 && LAT_CONFIG== 1 were retained, using the gtselect and gtmktime tasks, respectively. The region of interest was defined as a 10° radius centred on Ton 599. The source model included all sources listed in the *Fermi* LAT Third Source Catalogue, as well as Galactic and extragalactic diffuse emission templates from gll_iem_v07.fits and iso_P8R3_SOURCE_V3_v1.txt, respectively. Only the parameters of background sources within the inner 10° region and the normalization of the diffuse templates were allowed to vary during the
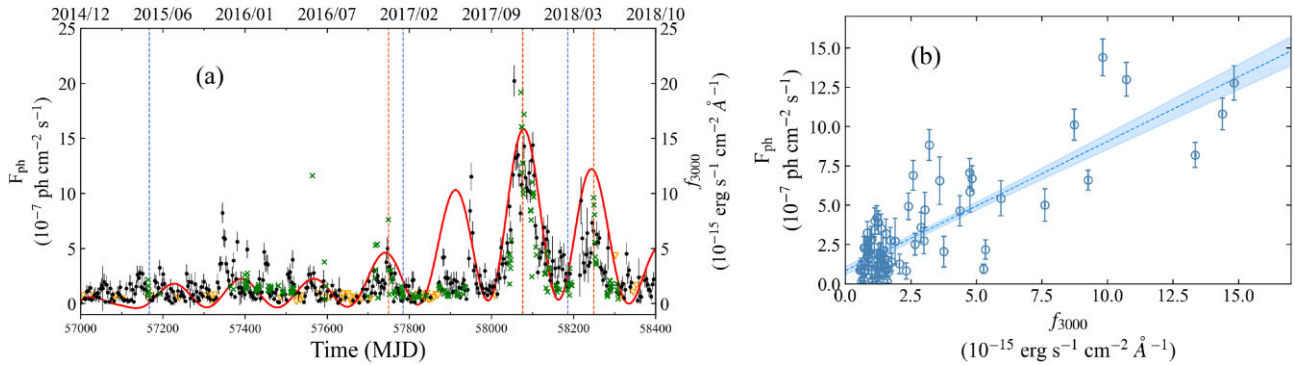
Figure 4. Left (a): The γ-ray and optical light curve of Ton 599. The black dots represent a 3-d binned light curve at γ-ray energies of 0.1–100 GeV, the yellow downwards triangles indicate flux upper limits, and the green crosses stand for the continuum flux density at 3000 Å. The red modulated sinusoidal curve, with a period of 176.80 ± 27.27 d, highlights the modulation in the light curve. Vertical dashed lines indicate the turn-on (blue) and turn-off (orange) events at different times. Right (b): The correlation between the continuum flux density at 3000 Å (f_{3000}) and the γ-ray photon flux shown in the left panel. The optical data were binned in 3-d intervals to match the cadence of the γ-ray light curve. A linear fit yields the relation $F_{\rm ph} = (0.82 \pm 0.06) f_{3000} - (0.83 \pm 0.01)$, with $r = 0.83$ and a p-value $< 10^{-6}$. The shaded blue region represents the 1σ uncertainty of the fit.

analysis, while all other parameters were fixed to their catalogue values. Light curves were generated using a 3-d binning interval, using a standard binned maximum likelihood analysis. This binning interval was chosen to balance temporal resolution with sufficient signal in most bins, to effectively capture flux variations. For time bins with low test statistic (TS) values (< 10), 95 per cent confidence limits were calculated using the `pyLikelihood UpperLimits` tool.

Fig. 4(a) displays the γ-ray and optical light curves of Ton 599. The black dots represent the 3-d binned γ-ray flux in the 0.1–100 GeV energy range, the yellow downward triangles denote the corresponding upper limits, and the green crosses indicate the f_{3000}. Fig. 4(b) shows the correlation between f_{3000} and the γ-ray photon flux. A linear fit yields the relation $F_{\rm ph} = (0.82 \pm 0.06) f_{3000} - (0.83 \pm 0.01)$, with $r = 0.83$ and a p-value $< 10^{-6}$. This suggests a strong correlation between the γ-ray and optical variability in Ton 599.

2.4 Searching for the γ-ray periodicity

To robustly identify significant periodic components in the γ-ray light curve, three different methods are employed in this work:

(a) The Weighted Wavelet Z-transform (WWZ; G. Foster 1996) is a versatile and widely adopted tool for analysing unevenly sampled astronomical time series. It provides a simultaneous representation of both frequency and temporal variations in a contour map. In the case of non-stationary or transient periodic signals, WWZ can reveal how the signal evolves over time through changes in the WWZ power. For further details and applications of this technique, see for example, G. Foster (1996), T. An et al. (2013), G. Bhatta et al. (2016), A. Sarkar et al. (2020), X.-P. Li et al. (2021), A. Roy et al. (2022), and J. Chen et al. (2024).

(b) The Lomb–Scargle Periodogram (LSP; N. R. Lomb 1976; J. D. Scargle 1982) is a widely used technique in time-domain astronomy for identifying and characterizing periodic signals in unevenly sampled time series. This method estimates the Fourier power spectrum efficiently and allows detection of possible periodic components in observational data. The WWZ and LSP methods have often been applied together to search for QPOs in light curves (e.g. G. Bhatta et al. 2016; G. Bhatta 2017; P.-F. Zhang et al. 2017; P.-f. Zhang et al. 2017a; J. Zhou et al. 2018; A. C. Gupta et al. 2019; J. Otero-Santos et al. 2020; X.-P. Li et al. 2021; A. Sarkar et al. 2021; A. Tripathi et al. 2021; A. Roy et al. 2022; Q.-B. Sun et al. 2023a, b).

(c) The Continuous Wavelet Transform (CWT[4]; C. Torrence & G. P. Compo 1998) decomposes the light curve by convolving it with a complex mother wavelet (e.g. Morlet wavelet) at different scales and times. The resulting complex coefficients have real and imaginary parts corresponding to different phase components, and their modulus $|W(a, b)|$ represents the signal amplitude, with $|W(a, b)|^2$ giving the power. Unlike the LSP, which provides only global power, or WWZ, which gives discrete time–frequency power, CWT yields continuous amplitude variations over time. This method has been widely applied to studies of astrophysical variability (e.g. C. Torrence & G. P. Compo 1998; T. Hovatta, H. J. Lehto & M. Tornikoski 2008; A. C. Gupta, A. K. Srivastava & P. J. Wiita 2009; L. C.-C. Lin et al. 2015; A. Ghosh, L. C. Gallo & A. G. Gonzalez 2023; H. X. Ren et al. 2023; Z.-H. Chen & Y. Jiang 2024; J. Otero-Santos et al. 2024; Q.-B. Sun et al. 2025).

These techniques are widely used to search for variability periodicity. Among them, the REDFIT[5] method is used to estimate the significance of the detected periodic signals by modelling the red-noise background, and light-curve simulations are also conducted to strengthen the robustness of the periodicity detection (M. Schulz & M. Mudelsee 2002).

In our WWZ analysis, we explored a frequency range from 0.002 to 0.018 d^{-1}, enabling the detection of QPOs on time-scales spanning from a few weeks to several months. A frequency step size of 0.0001 d^{-1} was used to ensure adequate resolution. The decay parameter was set to $c = 0.001$, which provides a balanced compromise between temporal and spectral resolution. As shown in Fig. 5, the left panel presents the WWZ power, and the right panel shows the time-averaged WWZ power derived from the γ-ray light curve in the MJD 57000–58400. A distinct peak appears at a period of 183.28 ± 17.73 d. The uncertainty in this periodicity is estimated from the half-width at half-maximum (HWHM) of the Gaussian profile fitted to the peak in the WWZ power.

For comparison, we also applied the LSP to the γ-ray light curve binned in 3-d intervals. As shown by the black curve in the Fig. 5, the periodogram result is in strong agreement with the time-averaged WWZ power, revealing a possible QPO with a period of 182.96 ± 15.83 d. Similar to the WWZ method, the uncertainty in
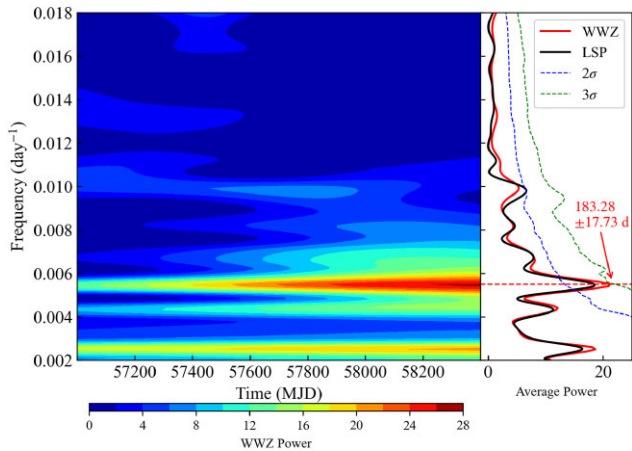
[4] https://github.com/regeirk/pycwt
[5] https://www.manfredmudelsee.com/soft/redfit/index.htm

Figure 5. Left panel: The WWZ power calculated from the γ-ray light curve in the MJD 57000–58400. Right panel: The time-averaged WWZ and LSP power spectra derived from the γ-ray light curve in the MJD 57000–58400. The red and black lines represent the averaged WWZ and LSP power, respectively. The blue and green dashed lines indicate the 2σ and 3σ significance levels, derived from 10^4 simulated light curves. The simulations reveal a periodic signal with a period of 183.28 ± 17.73 d detected by WWZ, reaching a significance level of 3σ.

the detected period was estimated using the HWHM of a Gaussian fit to the corresponding power peak. The results obtained with the CWT method are discussed in Section 2.6.

2.5 Significance estimation

Due to the fact that the variability of blazars typically exhibits frequency-dependent noise characteristics, spurious periodic signals can easily appear in periodograms. These false signals may be mistakenly interpreted as genuine periodicities, particularly at low frequencies (e.g. W. H. Press 1978; S. Vaughan et al. 2003, 2016; S. Vaughan 2005; G. Bhatta et al. 2016; G. Bhatta 2017; X.-P. Li et al. 2017, 2018, 2021; P.-F. Zhang et al. 2017; P.-f. Zhang et al. 2018). Such random fluctuations arising from stochastic processes are often well approximated by a power spectral density (PSD) that follows a power-law form, $P(f) \propto f^{-\alpha}$, where $P(f)$ is the power at temporal frequency f and α is the spectral index. This implies that when blazar light curves follow such a power-law PSD with $\alpha > 0$, significant variations tend to occur at lower frequencies, potentially resulting in artificial peaks in the periodogram. Specifically, this underlying noise is categorized as red noise when $1 < \alpha \leq 2$, and as flicker noise when $\alpha = 1$. In contrast, noise with a flat PSD ($\alpha = 0$) is referred to as white noise. Consequently, it is essential to properly account for such coloured noise when analysing variability features.

To assess the significance of the possible QPO signals detected in Ton 599, we constructed a coloured noise background through extensive Monte Carlo (MC) simulations. Assuming that a simple power-law model can adequately approximate the intrinsic red-noise PSD of the light curve, we estimated the power spectral index α by fitting a linear function to the logarithmic LSP, following the method described by S. Vaughan (2005). Based on the best-fitting PSD, we obtained a slope of $\alpha = 1.16 \pm 0.02$. Using this result, we simulated 10 000 light curves with the same mean, standard deviation, temporal coverage, and time resolution as the original 3-d binned γ-ray data.
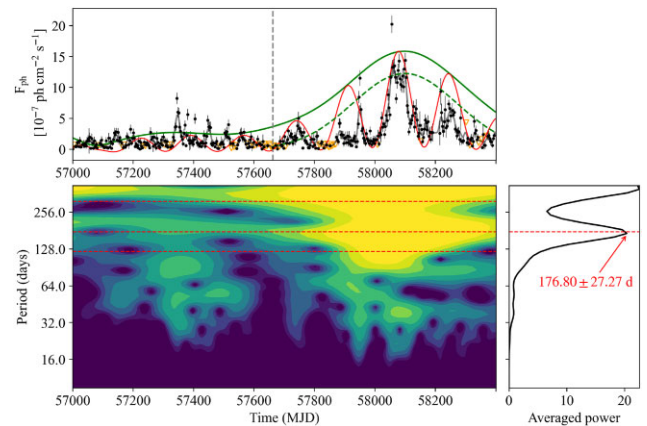

Figure 6. Detection of the quasi-periodic oscillation signal: Top panel: The γ-ray light curve and flux upper limits (95 per cent confidence level; yellow downwards triangles) are displayed, with a red curve representing the modulated 176.80 ± 27.27 d QPO and a green curve indicating the amplitude. We fitted the amplitude peak with a single Gaussian function centred at its maximum. The left limit of the fit is marked by a grey dashed line. To isolate the burst component, we subtracted the baseline level (estimated from the minimum value within the fitting range) from the fitted overall amplitude. The fit, shown as a green dashed line, yields $R^2 = 0.97$ with FWHM of ~ 400 d. Bottom left panel: The CWT power for the γ-ray light curve is presented, with red dashed lines indicating the carrier and sideband periods (frequencies) generated by the modulation, specifically at 121.95, 176.80, and 312.50 d. Bottom right panel: The black curve represents the time-averaged CWT power.

Each of these simulated light curves was analysed using the same WWZ procedures and parameters as those applied to the observed data in Section 2.4. The distribution of the time-averaged WWZ powers derived from the simulations was used to determine the local significance levels of power peaks in the observed WWZ spectrum. As illustrated in the Fig. 5, the blue dashed and green dashed lines represent the 2σ and 3σ confidence levels, respectively.

2.6 Amplitude-modulated QPOs

To investigate the frequency, amplitude, and phase evolution of the γ-ray light curve over time, we performed a time-frequency analysis using the CWT. Before applying the CWT, we first smoothed the 3-d binned γ-ray light curve using a Gaussian kernel with a standard deviation of 1.5 d. This pre-processing step was intended to suppress noise and enhance the visibility of potential periodic structures. The resulting smoothed light curve is shown as the grey line in the top panel of Fig. 6.

We then applied the CWT using the Morlet wavelet with a central frequency parameter of $\omega_0 = 6$, a commonly adopted value that balances time and frequency resolution in wavelet analysis (M. Farge 1992; C. Torrence & G. P. Compo 1998). Small variations in ω_0 (e.g. ± 1) do not significantly affect the resulting features. The CWT computes a convolution between the signal and the wavelet basis functions, producing complex wavelet coefficients that capture both amplitude and phase variations as a function of time and frequency. The results of this analysis are presented in the Fig. 6, where both the time-period spectrum (bottom left panel) and the period-folded power spectral density (bottom right panel) consistently indicate the presence of the 176.80 ± 27.27 d QPO, spanning the observation window from MJD 57000 to MJD 58400. Similarly, the uncertainty

in the detected period was estimated using the HWHM of a Gaussian fit to the corresponding power peak.

Although the periods identified by WWZ (183.28 ± 17.73 d), LSP (182.96 ± 15.83 d), and CWT (176.80 ± 27.27 d) show slight differences, they are all consistent within their respective uncertainties. These small discrepancies arise naturally from differences in the sensitivity and resolution of each method. Among the three methods, only CWT provides direct access to both amplitude and phase variations over time, making it particularly suitable for studying amplitude modulation. While WWZ also offers time–frequency localization, it does not provide explicit amplitude evolution curves. In contrast, LSP lacks time resolution altogether. Since our subsequent analysis focuses on the amplitude evolution of the periodic signal over time, we adopt the period obtained from the CWT, which is therefore better suited for this purpose.

The top panel of Fig. 6 shows the γ-ray light curve. The green solid line represents the amplitude variation corresponding to the 176-d QPO, where a distinct outburst in amplitude is clearly visible. We fitted the amplitude burst with a single Gaussian function centred at its maximum. The left limit of the fit is marked by a grey dashed line. To isolate the burst component, we subtracted the baseline level (estimated from the minimum value within the fitting range) from the fitted overall amplitude. The fit, shown as a green dashed line, yields a coefficient of determination $R^2 = 0.97$, with a full width at half maximum (FWHM) of ~ 400 d. We adopt this FWHM as the duration of the amplitude outburst, i.e. an amplitude modulation (AM) of ~ 400 d. This is because the FWHM provides a well-defined and symmetric measure of the main part of the outburst, avoiding uncertainties in selecting arbitrary start and end points. By modelling the 176-d QPO as a sine function and multiplying it by the amplitude variation, we obtain the red solid line, which represents the 176-d QPO after correcting for the AM effect.

The observed 176-d QPO exhibits a variable amplitude because of the influence of a long-term burst. This corresponds to a mathematical form of AM, where the modulation induces fluctuations in the QPO amplitude and introduces additional frequency components in the power spectrum (R. N. Bracewell 1966). A QPO functional form is given by:

$$F(t) = A_{\mathrm{QPO}}(t) \cos(2\pi f_{\mathrm{QPO}} t),$$

where A_{QPO} is the amplitude and f_{QPO} is the frequency. When the QPO amplitude is modulated by a burst characterized by

$$A_{\mathrm{QPO}}(t) = A_0 + A_{\mathrm{burst}} \cos(2\pi f_{\mathrm{burst}} t),$$

where A_0 is the base amplitude, A_{burst} is the burst amplitude, and f_{burst} is the burst frequency, the total flux becomes:

$$F(t) = [A_0 + A_{\mathrm{burst}} \cos(2\pi f_{\mathrm{burst}} t)] \cos(2\pi f_{\mathrm{QPO}} t).$$

Expanding this expression yields

$$F(t) = A_0 \cos(2\pi f_{\mathrm{QPO}} t)$$
$$+ \frac{A_{\mathrm{burst}}}{2} \left[\cos\left(2\pi(f_{\mathrm{QPO}} + f_{\mathrm{burst}})t\right) + \cos\left(2\pi(f_{\mathrm{QPO}} - f_{\mathrm{burst}})t\right) \right].$$

This expansion indicates that, in addition to the original QPO frequency f_{QPO}, two new sideband frequencies $f_{\mathrm{QPO}} - f_{\mathrm{burst}}$ and $f_{\mathrm{QPO}} + f_{\mathrm{burst}}$ appear in the signal due to the burst's modulation. In Fig. 6, the wavelet analysis of the γ-ray light curve of Ton 599 reveals a 176-d QPO and its associated amplitude variation. A prominent modulation signal appears in the amplitude variation, modelling the long-term burst with a single Gaussian. The burst duration, measured as the full width at half maximum, is ~ 400 d.

We obtain the carrier period (176-d) and the sideband periods (122 and 314-d) generated by the modulation, as shown by the red dashed lines in the power spectrum. However, these two sideband frequencies are obtained from the analytical expression rather than from the CWT data modelling. In the power spectrum, the power at these sideband frequencies is not very prominent: the ~ 314-d signal shows some excess power, while the ~ 122-d feature is much weaker. This weakness is expected, since sideband signals generally appear with lower amplitudes compared to the main QPO peak, and their detectability can be further reduced by noise and limited data sampling.

3 DISCUSSIONS

3.1 QPOs and helical jet interpretation in Ton 599

The presence of QPOs in the rapid and high variability of blazars is extremely interesting, and many studies have focused on understanding their physical origin. Various mechanisms have been proposed to explain QPOs at different time-scales.

For year-long QPOs, a gravitationally bound binary SMBH system (M. C. Begelman, R. D. Blandforth & M. J. Rees 1980; J. E. Barnes & L. Hernquist 1992) with a total mass of $\sim 10^8 \, \mathrm{M_\odot}$ is a possible explanation. Periodicities induced by binary SMBH have time-scales ranging from ~ 1 to ~ 25 yr (S. Komossa 2006; F. M. Rieger 2007), and this model has been applied to numerous year-long QPOs (e.g. M. Ackermann et al. 2015; M. Charisi et al. 2015; A. Sandrinelli et al. 2016a; H. Zhang, F. Wu & B. Dai 2023; H. Zhang et al. 2025). The most well-known case is the ~ 12-yr QPO of OJ 287, which has been successfully explained by the binary SMBH model (M. J. Valtonen et al. 2008; C. Villforth et al. 2010). In addition, other models have also been proposed to account for long-term QPOs, such as jet precession driven by a secondary black hole in a non-coplanar orbit (G. E. Romero et al. 2000; M. Liska et al. 2018), or Lense–Thirring precession of the accretion disc (L. Stella & M. Vietri 1998).

For short-term QPOs, several physical models have been proposed. One possibility is the presence of hotspots rotating at the innermost stable circular orbit (ISCO) of the central SMBH, which can modulate the seed photon field for external inverse Compton (IC) scattering in the jet and thereby imprint periodic variations on the γ-ray emission (X. H. Zhang & G. Bao 1991; A. C. Gupta et al. 2009). A. Roy et al. (2022) reported two transient γ-ray QPOs in the TeV blazar PKS 1510–089, with periods of ~ 3.6 and 92 d. By comparing the black hole masses inferred from these periods with independent estimates, they concluded that the hotspot scenario is consistent with the 3.6-d QPO but cannot reasonably account for the 92-d signal. Another mechanism involves magnetic reconnection events that create nearly equally spaced magnetic islands inside the jet, periodically enhancing the flux and producing transient QPOs (C.-Y. Huang et al. 2013; A. Shukla et al. 2018). A. Shukla et al. (2018) explained the extremely fast ~ 5 min variability observed during the CTA 102 outburst using a magnetic reconnection process.

In the γ-ray light curve of Ton 599, we detect a transient QPO with an observed period of ~ 176 d. To interpret this modulation, we consider the helical jet scenario (M. Villata & C. M. Raiteri 1999; P. Mohan & A. Mangalam 2015; E. Sobacchi et al. 2017; J. Zhou et al. 2018), in which the emission region (or blob) within the jet moves along a helical path due to large-scale magnetic fields or dynamical instabilities. In this framework, the viewing angle of the emitting
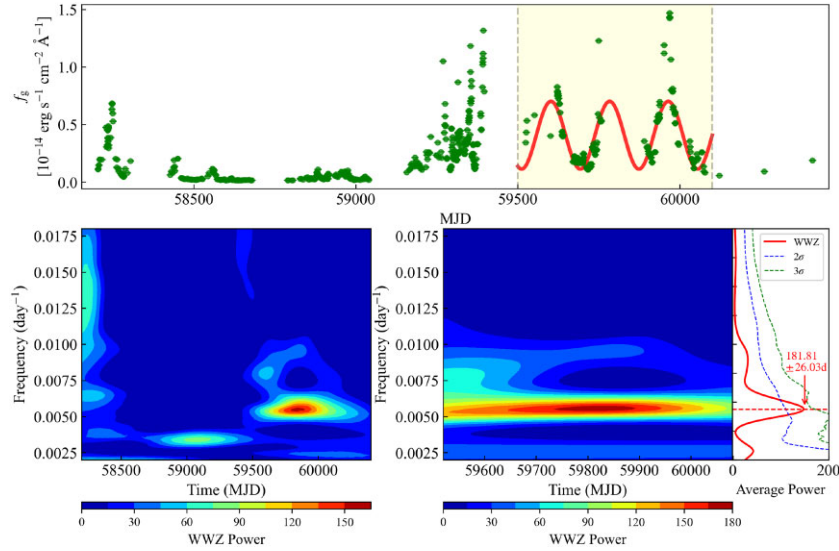
Figure 7. Top panel: The *g*-band flux light curve (MJD 58200–60410) converted from ZTF magnitudes. The red sinusoidal curve (with a period of 181 d) is overplotted to indicate the modulation in the light curve. Bottom panels: Left – the WWZ power for the whole light curve shown in the top row. Middle – the WWZ power calculated for the time interval MJD 59500–60100, corresponding to the possible periodic modulation. Right – the time-averaged WWZ power, together with the 2σ (blue dashed) and 3σ (green dashed) significance curves derived from light curve simulations.

blob varies with time according to

$$\cos\theta = \cos\phi\cos\psi + \sin\phi\sin\psi\cos\left(2\pi t/P_{\mathrm{obs}}\right), \qquad (3)$$

where ϕ is the pitch angle of the helical trajectory relative to the jet axis, ψ is the angle between the jet and the observer's line of sight, and P_{obs} is the observed period. The intrinsic physical period P is related to the observed period by the relativistic projection effect:

$$P = P_{\mathrm{obs}}/(1 - \beta\cos\phi\cos\psi), \qquad (4)$$

where $\Gamma = (1 - \beta^2)^{-1/2}$ is the bulk Lorentz factor, β is the velocity in units of the speed of light. When the typical parameters for FSRQ-type blazars ($\phi = 2°$, $\psi = 5°$, $\Gamma = 20$) suggested in previous works (E. Sobacchi et al. 2017; J. Zhou et al. 2018; J. Chen et al. 2022) are adopted for the 176-d γ-ray QPO observed in Ton 599, we obtain that the intrinsic physical period is $P \approx 85.17$ yr. The distance traveled by the blob in one cycle is $D = c\beta P\cos\phi \approx 26.07$ pc, and the total projected distance over 7 cycles is $D_{\mathrm{p}} = 7D\sin\psi \approx 15.90$ pc.

For comparison, J. Chen et al. (2024) reported five transient QPOs in blazars: 4C+01.02, PKS 0336–01, PKS 0402–362, PKS 0537–441, PKS 1424–41, and PKS 1510–089. Their observed periods range from ∼55 to 341 d, with corresponding intrinsic physical periods P of ∼13 to 165 yr, distances D in the jet of ∼4 to 50 pc, and total projected distances D_{p} of ∼2.5 to 26 pc (see table 3 in J. Chen et al. 2024). Our derived values for Ton 599 ($P \sim 85.17$ yr, $D \sim 26.07$ pc, $D_{\mathrm{p}} \sim 15.90$ pc) fall within these ranges, supporting the helical jet scenario as a viable explanation for the observed 176-d γ-ray QPO.

The helical jet interpretation can be further tested with multiwavelength monitoring, since such QPOs are expected to reappear (J. Zhou et al. 2018). Notably, J. Chen et al. (2024) reported a repeated transient QPO in PKS 0537–441: a ∼55-d QPO observed at MJD 56803–57183 reappeared within the error range about 450 d later at MJD 57636–58036. This recurrence suggests that the spiralling emission region (or blob) within the jet is reproducible, modulating the γ-ray emission in a consistent manner. If the 176-d QPO in Ton

599 is indeed caused by a helical jet, similar QPO signatures should also be observable at other times and in other wavebands.

We employed the ZTF, a wide-field optical time-domain survey carried out with the 48-inch Schmidt Telescope at Palomar Observatory, which regularly monitors the northern sky (E. C. Bellm et al. 2019; F. J. Masci et al. 2019). Its photometry is calibrated in the AB system, where a magnitude of zero corresponds to a reference flux density of 3631 Jy (F. J. Masci et al. 2019). For Ton 599, we collected photometric data from MJD 58 200 to MJD 60410, with 680 points in the *g* band, 618 in the *r* band, and 165 in the *i* band. To improve data reliability, only measurements with $catflags = 0$ were retained, and the magnitudes were converted to flux densities for subsequent analysis.

We focused on the *g*-band data in our analysis, and the corresponding light curve is shown in the top panel of Fig. 7. The bottom panels (left) present the WWZ power spectrum of the entire *g*-band light curve, where a periodic signal of ∼181 d is revealed during the interval MJD 59500–60100. The WWZ method applied to the light curve during MJD 59500–60100 provided clearer results (bottom panels, middle), highlighting the modulation. The bottom panels (right) display the time-averaged WWZ power together with the 2σ (blue dashed) and 3σ (green dashed) significance curves, indicating that the detected periodicity reaches a confidence level above 2σ. These results provide further evidence supporting the helical jet scenario in Ton 599.

Actually, relativistic jets may not be homogeneous but instead composed of multiple relativistic blobs or sub-jets (J. E. Conway & D. W. Murphy 1993). These sub-jets, moving along helical paths, can generate localized flares and are likely responsible for the rapid, small-scale variability observed in Ton 599. These small outbursts represent short-term variations, while the 176-d (or ∼181-d) QPO reflects their periodic clustering. Furthermore, the 400-d AM governs the long-term fluctuation in the intensity of both the small outbursts and the QPO. This long-term modulation may arise from jet precession or secular changes in the accretion flow, further linking the geometry and dynamics of the jet to the QPO behaviour.
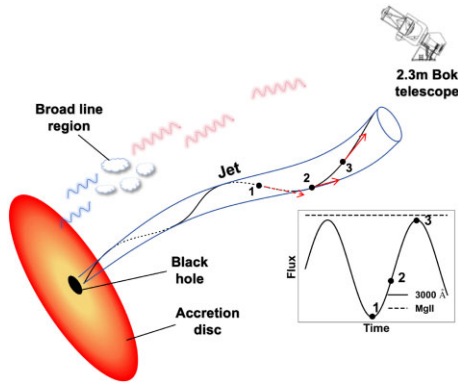
Figure 8. Schematic diagram of a curved jet producing periodic emission. As the emitting blob moves along a helical path in the jet, its position changes (such as at points 1, 2, and 3), causing the viewing angle to periodically vary relative to the observer. The BLR gases are primarily influenced by the ionizing emission from the accretion disc, rather than the jet.

3.2 Changing-look from jet geometry

Since the first CL phenomenon was identified by E. Y. Khachikian & D. W. Weedman (1971), the number of known CL AGNs has increased significantly. Despite this progress, the underlying mechanism driving these transitions remains an open question. Possible explanations include changes in accretion rates (M. V. Penston & E. Perez 1984; M. Elitzur, L. C. Ho & J. R. Trump 2014), changing obscurations (M. Nenkova et al. 2008a, b), or tidal disruption events (TDEs; M. Eracleous et al. 1995; A. Merloni et al. 2015; P. K. Blanchard et al. 2017). In these mechanisms, the (dis)appearance of BELs being closely related to the (dis)appearance of enhanced continuum emission. Our findings in Ton 599 are obviously different from this relationship, as we found that the BELs appear at lower continuum flux density and disappear at higher flux levels. Based on the repeated spectral transitions and the consistency between the continuum and γ-ray variations, we suspect that the plausible explanation is likely a geometrical origin.

In the spectra transitions of Ton 599, although the continuum spectral flux exhibited significant changes, the variation in the BEL flux was not significant. This suggests that variations in the continuum flux density do not affect the Mg II emission line flux. Furthermore, the continuum flux density variations exhibit a strong correlation with the 176-day γ-ray QPO between MJD 57000 and 58400, indicating that the variations in continuum and γ-ray intensity share the same origin. For the multimonth QPO in the γ-ray light curve (J. Zhou et al. 2018; A. Sarkar et al. 2021; A. Roy et al. 2022), the curved jet model is a possible explanation (M. Villata & C. M. Raiteri 1999). In this model (see a schematic illustration in Fig. 8), a relativistic blob in the jet moves along a helical path towards us, causing periodic changes in the Doppler factor as the viewing angle varies. These changes regulate the observed optical continuum flux density and γ-ray flux. This helical structure could explain the observed periodic modulation and spectral transitions in Ton 599.

When the viewing angle is small, the beamed non-thermal radiation from the jet will outshine the BELs and causing them to appear weaker or even temporarily undetectable (turn-off). As the viewing angle increases, the continuum emission weakens, becoming comparable to the line flux, leading to a turn-on event. B. J. Wills et al.
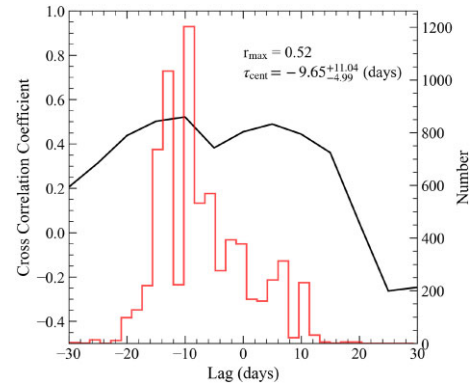

Figure 9. ICCF between the Mg II broad emission line flux and the 3000 Å continuum for Ton 599. The black curve shows the ICCF as a function of lag, with a maximum correlation coefficient of $r_{max} \sim 0.52$. The red histogram on the right axis shows the distribution of centroid lags τ_{cent} obtained from 7000 FR/RSS MC simulations, yielding a centroid lag of $\tau_{cent} \sim -9.7^{+11.1}_{-4.96}$ d.

(1983) previously reported that when Ton 599 is bright, its optical spectrum appears featureless like a BL Lac object; however, in the faint state, it exhibits emission lines typical of a quasi-stellar object (QSO). S. R. Patel et al. (2018) also observed that the Mg II line in Ton 599 becomes significantly diluted when the continuum flux density is high, resulting in a reduced EW. These unique characteristics distinguish Ton 599 from other CL AGNs, where BELs typically appear with increased continuum flux density. In comparison, Ton 599's behaviour suggests a more significant role of jet geometry and viewing angle effects. Similar findings have been reported for other blazars, including BL Lacertae (E. A. Corbett et al. 2000), AO 0235+164 (C. M. Raiteri et al. 2007), 3C 454.4 (C. M. Raiteri et al. 2008), OJ 248 (M. I. Carnerero et al. 2015), and CTA 102 (V. M. Larionov et al. 2016).

These special events suggest that the BLR gases in blazars are probably ionized by thermal radiation from the accretion disk, while they are only weakly affected by the beaming jet radiation. The study of these cases, including Ton 599, underscores the diversity of mechanisms driving CL events and highlights the importance of geometry in shaping AGN observations.

To further investigate the connection between the continuum and Mg II emission, we performed an interpolation cross-correlation function (ICCF; C. M. Gaskell & L. S. Sparke 1986; C. M. Gaskell & B. M. Peterson 1987; R. J. White & B. M. Peterson 1994) analysis between the 3000 Å continuum and the Mg II line flux. The time lag was determined using the ICCF centroid (τ_{cent}) around the peak, with uncertainties estimated through 7000 realizations of flux randomization/random subset sampling (FR/RSS) MC simulations (B. M. Peterson et al. 1998, 2004). Our results reveal a maximum correlation coefficient of $r_{max} \sim 0.52$ and a centroid lag of $\tau_{cent} \sim -9.7^{+11.10}_{-4.96}$ d (Fig. 9). The negative lag indicates that variations in the Mg II line generally precede those in the continuum, suggesting that the observed continuum is significantly influenced by emission from a more distant region, likely associated with the jet. The asymmetric uncertainties reflect the skewed distribution obtained from the MC simulations, implying that the lag could range roughly from -14.7 to $+1.4$ d. Despite the uncertainty, the negative centroid supports the scenario in which the continuum is strongly contaminated by jet emission, indicating that Mg II-based virial methods are not suitable for estimating black hole masses in Ton 599.

3.3 The Baldwin effect

The observed anticorrelation between $\log \mathrm{EW_{MgII}}$ and $\log L_{3000}$ (Fig. 3, left panel) is consistent with the results reported in numerous previous studies (e.g. J. Kovačević, L. Č. Popović & M. S. Dimitrijević J. Kovačević et al.; M. Dietrich et al. 2002; L. Huang et al. 2023; V. Patiño Álvarez et al. 2016; N. Rakić et al. 2017; O. Shemmer & S. Lieber 2015; J. C. Shields 2007; H. Xiao et al. 2022), and it represents a hallmark of the BEff (J. A. Baldwin 1977). Since its discovery, the BEff has been widely detected across both broad and narrow emission lines in the UV/optical regime (M. Dietrich et al. 2002; J. C. Shields 2007; J. Kovačević et al. 2010), with the slope becoming steeper for lines of higher ionization potential (W. Zheng & M. A. Malkan 1993).

This trend has stimulated numerous theoretical explanations. For instance, R. Mushotzky & G. J. Ferland (1984) proposed that the BEff arises from a luminosity-dependent ionization parameter and a possible decrease in BLR covering factor with increasing luminosity, which explains why the BEff is prominent in CIV but weak or absent in Ly α and other hydrogen lines. H. Netzer (1985) suggested that BEff can be naturally explained by geometric effects, where anisotropic emission from thin accretion discs combined with nearly isotropic line emission leads to the observed anticorrelation between line EW and continuum luminosity. A. L. Kinney, A. R. Rivolo & A. P. Koratkar (1990) confirmed the BEff as a genuine correlation, extended it to Ly α, and noted that variability largely accounts for the observed scatter. Even the impact of accretion rate and black hole mass has been investigated as possible drivers of the BEff (Y. Xu et al. 2008; W.-H. Bian et al. 2012). The most accepted explanation is that as luminosity increases, the ionizing continuum becomes softer, reducing the number of high-energy photons in luminous AGNs (W. Zheng & M. A. Malkan 1993). In particularly, the CIV BEff, has been proposed as a potential cosmological probe (L. Huang et al. 2023).

We obtained a BEff slope of -0.92 ± 0.02 for the relation between $\log \mathrm{EW_{MgII}}$ and $\log L_{3000}$ in Ton 599, which is significantly steeper than those typically derived from a large sample. For comparison, V. Patiño Álvarez et al. (2016) analysed 96 core-jet blazars and found slopes of -0.20 for Mg II and -0.21 for C IV. H. Xiao et al. (2022) based on single-epoch observations of a large number of blazars reported slopes of -0.24 ± 0.03 for Mg II and -0.25 ± 0.05 for C IV. The slopes derived from multi-epoch observations of individual sources are systematically steeper than those obtained from single-epoch ensemble studies (A. L. Kinney et al. 1990; K. M. Gilbert & B. M. Peterson 2003; H. Guo & M. Gu 2014; N. Rakić et al. 2017). Specifically, A. L. Kinney et al. (1990) reported BEff slopes ranging from -0.36 to -0.90 for C IV and from -0.38 to -0.75 for Ly α in 3C 273, ESO 141−G55, NGC 4593, Mrk 509, NGC 3783, NGC 5548, and 3C 120, while the overall fit to these sources yielded much shallower slopes of -0.17 ± 0.04 for C IV and -0.12 ± 0.05 for Ly α. Our result for Ton 599 is therefore consistent with the steeper slopes typically found in multi-epoch studies.

Moreover, it is found that blazars show steeper BEff slopes than radio-quiet quasars (V. Patiño Álvarez et al. 2016). H. Xiao et al. (2022) suggested that this steepening may arise from IC scattering of broad line photons by the relativistic jet. In this work, we find that the variations of $\mathrm{EW_{MgII}}$ with continuum luminosity are most likely driven by geometric effects of the jet. While the reduction of broad line photons can indeed contribute to smaller EWs, an equally important factor is that when the beamed continuum brightens rapidly, the line flux produced outside the jet is only weakly affected by beaming (E. A. Corbett et al. 2000; C. M. Raiteri et al. 2007,

2008; M. I. Carnerero et al. 2015; V. M. Larionov et al. 2016), causing the EW to drop sharply. This naturally leads to a steeper BEff and, in extreme cases, even to the disappearance of broad emission lines, giving rise to CL phenomena. It remains unclear whether IC depletion of BLR photons or direct dilution of line flux by the beamed continuum plays the dominant role in this steepening.

As shown in Fig. 3, the correlation between $\log \mathrm{EW_{MgII}}$ and $\log L_{3000}$ has a slope of -0.92, with $r = -0.97$ and $p < 10^{-6}$. In contrast, $\log \mathrm{EW_{MgII}}$ and $\log L_{\mathrm{MgII}}$ show no correlation ($r = -0.05$, $p = 0.46$), with $\log L_{\mathrm{MgII}}$ remaining nearly constant around $43.65 \, \mathrm{erg \, s^{-1}}$. Furthermore, the optical continuum flux at 3000 Å exhibits strong variability, with a normalized excess variance of $F_{\mathrm{var}} = 1.089$, whereas the Mg II flux varies with a much smaller amplitude of $F_{\mathrm{var}} = 0.194$. If IC scattering of broad line photons played a major role in the BEff of Ton 599, significant variability in the line flux would be expected. Instead, although the line flux does vary, the continuum varies much more strongly, indicating that in Ton 599 the decrease in $\mathrm{EW_{MgII}}$ is primarily caused by dilution of the emission line by the beamed continuum.

4 SUMMARY

We conducted a detailed analysis of the time series of the optical spectra and corresponding γ-ray light curve of Ton 599 to investigate its spectral emission changes, also known as CL events, and the potential driving mechanisms. The results reveal significant variations in the EW of the BELs, which is primarily driven by fluctuations in the continuum rather than by changes in the BEL flux.

Additionally, the optical continuum flux density exhibits a strong correlation with the γ-ray flux, with no significant time delay detected between the two bands (I. Liodakis et al. 2018, 2019; R. Prince 2019; T. Jaeger et al. 2023). This suggests that the variability in both bands originates from closely related processes, possibly within a single emission region (B. Rajput et al. 2024) or due to linked dynamical mechanisms.

Time-frequency analysis of the γ-ray light curve reveals the presence of a ∼176-d QPO during MJD 58200–59200. Notably, this QPO is amplitude-modulated on a characteristic time-scale of ∼400 d. This dual time-scale behaviour points to the presence of a complex modulation mechanism, possibly driven by geometric effects or intrinsic dynamical processes within the system. A similar QPO with a period of ∼181 d is also detected in the optical g-band light curve during MJD 58200–60410, providing further support for the interpretation that these periodicities in Ton 599 are driven by jet geometry.

Our findings indicate that the jet's helical structure could play a crucial role in driving CL events in some AGNs. In particular, these results support the traditional unified model by emphasizing the importance of jet geometry and viewing angle in shaping observed variability. This insight enhances our understanding of the complex structure and underlying physical mechanisms of AGN jets, and offers crucial support for refining the unified model of AGNs. However, it is important to acknowledge the complexity of CL phenomena in AGN. Our explanation is based on the relationship between continuum variations and QPO time-scales in the blazar Ton 599. While other mechanisms (such as changes in accretion rate, obscuration, or TDEs) may still account for CL phenomena in other types of AGNs, our findings definitively rule them out in Ton 599. The optical data's sparsity further limits the temporal resolution of our findings, necessitating more dense and long-term monitoring to fully disentangle the contributions of different physical processes.

ACKNOWLEDGEMENTS

DATA AVAILABILITY

The SO[6] optical spectra, ZTF[7] *g*-band photometric data, and *Fermi* LAT[8] data used in this work can be obtained from public archives. The optical spectra were observed by SO at the University of Arizona as part of the Ground-based Observational Support of the *Fermi* Gamma-ray Space Telescope program. We provide all the fitting results for the 191 spectra of Ton 599 in the supplementary material. The corresponding author will share all other data underlying this article upon reasonable request.

[6] https://james.as.arizona.edu/~psmith/Fermi/
[7] https://irsa.ipac.caltech.edu/Missions/ztf.html
[8] https://fermi.gsfc.nasa.gov/ssc/data/access/

REFERENCES

Abdo A. A. et al., 2010, ApJS, 188, 405
Ackermann M. et al., 2015, ApJ, 813, L41
Alvarez Crespo N. et al., 2016, AJ, 151, 32
An T., Baan W. A., Wang J.-Y., Wang Y., Hong X.-Y., 2013, MNRAS, 434, 3487
Baldwin J. A., 1977, ApJ, 214, 679
Barnes J. E., Hernquist L., 1992, ARA&A, 30, 705
Begelman M. C., Blandford R. D., Rees M. J., 1980, Nature, 287, 307
Bellm E. C. et al., 2019, PASP, 131, 018002
Bhatta G., 2017, ApJ, 847, 7
Bhatta G., Dhital N., 2020, ApJ, 891, 120
Bhatta G. et al., 2016, ApJ, 832, 47
Bian W.-H., Fang L.-L., Huang K.-L., Wang J.-M., 2012, MNRAS, 427, 2881
Blanchard P. K. et al., 2017, ApJ, 843, 106
Blandford R. D., König A., 1979, ApJ, 232, 34
Boroson T. A., Green R. F., 1992, ApJS, 80, 109
Boula S., Kazanas D., Mastichiadis A., 2019, MNRAS, 482, L80
Bracewell R. N., 1966, The Fourier Transform and Its Applications. Available at: https://api.semanticscholar.org/CorpusID:18010056
Cardelli J. A., Clayton G. C., Mathis J. S., 1989, ApJ, 345, 245
Carnerero M. I. et al., 2015, MNRAS, 450, 2677
Chand K., Gopal-Krishna, 2025, MNRAS, 541, L52
Charisi M., Bartos I., Haiman Z., Price-Whelan A. M., Márka S., 2015, MNRAS, 454, L21
Chen G., Zheng Z., Zeng X., Zhang L., Xiao H., Liu X., Cui L., Fan J., 2024, ApJS, 271, 20
Chen J., Yi T., Gong Y., Yang X., Chen Z., Chang X., Mao L., 2022, ApJ, 938, 8
Chen J., Yu J., Huang W., Ding N., 2024, MNRAS, 528, 6807
Chen Z.-H., Jiang Y., 2024, A&A, 689, A35
Cohen R. D., Rudy R. J., Puetter R. C., Ake T. B., Foltz C. B., 1986, ApJ, 311, 135
Conway J. E., Murphy D. W., 1993, ApJ, 411, 89
Corbett E. A., Robinson A., Axon D. J., Hough J. H., 2000, MNRAS, 311, 485
Denney K. D. et al., 2014, ApJ, 796, 134
Dietrich M., Hamann F., Shields J. C., Constantin A., Vestergaard M., Chaffee F., Foltz C. B., Junkkarinen V. T., 2002, ApJ, 581, 912
Dong Q., Zhang Z.-X., Gu W.-M., Sun M., Zheng Y.-G., 2025, ApJ, 986, 160
Edelson R., Turner T. J., Pounds K., Vaughan S., Markowitz A., Marshall H., Dobbie P., Warwick R., 2002, ApJ, 568, 610
Elitzur M., 2012, ApJ, 747, L33
Elitzur M., Ho L. C., Trump J. R., 2014, MNRAS, 438, 3340
Eracleous M., Livio M., Halpern J. P., Storchi-Bergmann T., 1995, ApJ, 438, 610
Fan J. H., 2003, ApJ, 585, L23
Fan J. H., Lin R. G., Xie G. Z., Zhang L., Mei D. C., Su C. Y., Peng Z. M., 2002, A&A, 381, 1
Fan J.-H., Romero G. E., Wang Y.-X., Zhang J.-S., 2005, Chinese J. Astron. Astrophys., 5, 457
Fan J. H. et al., 2007, A&A, 462, 547
Farge M., 1992, Annu. Rev. Fluid Mech., 24, 395
Foschini L. et al., 2021, Universe, 7, 372
Foster G., 1996, AJ, 112, 1709
Fu Y., 2021, QSOFITMORE: a python package for fitting UV-optical spectra of quasars (v1.0.0). Zenodo. Available at: https://doi.org/10.5281/zenodo.4893734
Gaskell C. M., Peterson B. M., 1987, ApJS, 65, 1
Gaskell C. M., Sparke L. S., 1986, ApJ, 305, 175
Ghosh A., Gallo L. C., Gonzalez A. G., 2023, MNRAS, 524, 1478
Gierliński M., Middleton M., Ward M., Done C., 2008, Nature, 455, 369
Gilbert K. M., Peterson B. M., 2003, ApJ, 587, 123
Giommi P., Padovani P., Polenta G., Turriziani S., D'Elia V., Piranomonte S., 2012, MNRAS, 420, 2899
Guo H., Gu M., 2014, ApJ, 792, 33
Gupta A. C., Srivastava A. K., Wiita P. J., 2009, ApJ, 690, 216
Gupta A. C., Tripathi A., Wiita P. J., Kushwaha P., Zhang Z., Bambi C., 2019, MNRAS, 484, 5785
Ho L. C., Filippenko A. V., Sargent W. L. W., 1993, ApJ, 417, 63
Hogg D. W., 1999, preprint (arXiv:astro-ph/990511)
Hovatta T., Lehto H. J., Tornikoski M., 2008, A&A, 488, 897
Huang C.-Y., Wang D.-X., Wang J.-Z., Wang Z.-Y., 2013, Res. Astron. Astrophys., 13, 705
Huang L., Wang H., Gao Z., Zeng X., Chang Z., 2023, A&A, 674, A163
de Jaeger T. et al., 2023, MNRAS, 519, 6349
Jin J.-J. et al., 2023, ApJS, 265, 25
Kang S.-J., Ren S.-S., Zheng Y.-G., Wu Q., 2025, ApJ, 980, 213
Khachikian E. Y., Weedman D. W., 1971, ApJ, 164, L109
Kinney A. L., Rivolo A. R., Koratkar A. P., 1990, ApJ, 357, 338
Komossa S., 2006, Mem. Soc. Astron. Italiana, 77, 733
Kormendy J., Ho L. C., 2013, ARA&A, 51, 511
Kovačević J., Popović L. Č., Dimitrijević M. S., 2010, ApJS, 189, 15
Kushwaha P., Sarkar A., Gupta A. C., Tripathi A., Wiita P. J., 2020, MNRAS, 499, 653
Lachowicz P., Gupta A. C., Gaur H., Wiita P. J., 2009, A&A, 506, L17
Lainela M. et al., 1999, ApJ, 521, 561
Larionov V. M. et al., 2016, MNRAS, 461, 3047
Levy C., Sol H., Bolmont J., 2024, A&A, 689, A136

Li X.-P., Luo Y.-H., Yang H.-Y., Yang C., Cai Y., Yang H.-T., 2017, ApJ, 847, 8

Li X.-P., Luo Y.-H., Yang H.-Y., Yang C., Cai Y., Yang H.-T., Zhou L., Shan Y.-Q., 2018, Ap&SS, 363, 169

Li X.-P., Cai Y., Yang H.-T., Luo Y.-H., Yan Y., He J.-Y., Wang L.-S., 2021, MNRAS, 506, 1540

Li X.-P. et al., 2023, MNRAS, 519, 4893

Lin D., Irwin J. A., Godet O., Webb N. A., Barret D., 2013, ApJ, 776, L10

Lin L. C.-C., Hu C.-P., Kong A. K. H., Yen D. C.-C., Takata J., Chou Y., 2015, MNRAS, 454, 1644

Liodakis I., Romani R. W., Filippenko A. V., Kiehlmann S., Max-Moerbeck W., Readhead A. C. S., Zheng W., 2018, MNRAS, 480, 5517

Liodakis I., Romani R. W., Filippenko A. V., Kocevski D., Zheng W., 2019, ApJ, 880, 32

Liska M., Hesp C., Tchekhovskoy A., Ingram A., van der Klis M., Markoff S., 2018, MNRAS, 474, L81

Lomb N. R., 1976, Ap&SS, 39, 447

Mandal A. K. et al., 2021, MNRAS, 508, 5296

Masci F. J. et al., 2019, PASP, 131, 018003

McElroy R. E. et al., 2016, A&A, 593, L8

Merloni A. et al., 2015, MNRAS, 452, 69

Mignone A., Rossi P., Bodo G., Ferrari A., Massaglia S., 2010, MNRAS, 402, 7

Mishra H. D. et al., 2021, ApJ, 913, 146

Mohan P., Mangalam A., 2015, ApJ, 805, 91

Mushotzky R., Ferland G. J., 1984, ApJ, 278, 558

Nenkova M., Sirocky M. M., Ivezić Ž., Elitzur M., 2008a, ApJ, 685, 147

Nenkova M., Sirocky M. M., Nikutta R., Ivezić Ž., Elitzur M., 2008b, ApJ, 685, 160

Netzer H., 1985, MNRAS, 216, 63

Otero-Santos J. et al., 2020, MNRAS, 492, 5524

Otero-Santos J. et al., 2024, A&A, 686, A228

Padovani P. et al., 2017, A&A Rev., 25, 2

Palit B., Śniegowska M., Markowitz A., Różańska A., Farah J., Howell D. A., 2025, MNRAS, 540, L14

Patel S. R., Chitnis V. R., Shukla A., Rao A. R., Nagare B. J., 2018, ApJ, 866, 102

Patiño Álvarez V., Torrealba J., Chavushyan V., Cruz González I., Arshakian T., León Tavares J., Popovic L., 2016, Front. Astron. Space Sci., 3, 19

Peñil P., Otero-Santos J., Banerjee A., Buson S., Rico A., Ajello M., Adhikari S., 2025, A&A, 700, A208

Pena-Herazo H. A. et al., 2021, AJ, 161, 196

Penil P., Ajello M., Buson S., Domínguez A., Westernacher-Schneider J. R., Rico A., Adhikari S., Zrake J., 2025, MNRAS, 541, 2955

Penston M. V., Perez E., 1984, MNRAS, 211, 33P

Peterson B. M., Wanders I., Horne K., Collier S., Alexander T., Kaspi S., Maoz D., 1998, PASP, 110, 660

Peterson B. M. et al., 2004, ApJ, 613, 682

Press W. H., 1978, Comments Astrophys., 7, 103

Prince R., 2019, ApJ, 871, 101

Raimundo S. I., Vestergaard M., Koay J. Y., Lawther D., Casasola V., Peterson B. M., 2019, MNRAS, 486, 123

Raiteri C. M. et al., 2001, A&A, 377, 396

Raiteri C. M., Villata M., Capetti A., Heidt J., Arnaboldi M., Magazzù A., 2007, A&A, 464, 871

Raiteri C. M. et al., 2008, A&A, 491, 755

Raiteri C. M. et al., 2017, Nature, 552, 374

Rajput B., Mandal A. K., Pandey A., Stalin C. S., Max-Moerbeck W., Mathew B., 2024, MNRAS, 527, 11900

Rakić N., La Mura G., Ilić D., Shapovalova A. I., Kollatschny W., Rafanelli P., Popović L. Č., 2017, A&A, 603, A49

Ren G.-W., Zhang H.-J., Zhang X., Ding N., Yang X., Li F.-T., Yan P.-L., Xu X.-L., 2021a, Res. Astron. Astrophys., 21, 075

Ren G.-W., Ding N., Zhang X., Xue R., Zhang H.-J., Xiong D.-R., Li F.-T., Li H., 2021b, MNRAS, 506, 3791

Ren H. X., Cerruti M., Sahakyan N., 2023, A&A, 672, A86

Ricci C., Trakhtenbrot B., 2023, Nat. Astron., 7, 1282

Rieger F. M., 2007, Ap&SS, 309, 271

Romero G. E., Chajet L., Abraham Z., Fan J. H., 2000, A&A, 360, 57

Roy A., Sarkar A., Chatterjee A., Gupta A. C., Chitnis V., Wiita P. J., 2022, MNRAS, 510, 3641

Ruan J. J., Anderson S. F., Plotkin R. M., Brandt W. N., Burnett T. H., Myers A. D., Schneider D. P., 2014, ApJ, 797, 19

Sandrinelli A., Covino S., Dotti M., Treves A., 2016a, AJ, 151, 54

Sandrinelli A., Covino S., Treves A., 2016b, ApJ, 820, 20

Sandrinelli A., Covino S., Treves A., Holgado A. M., Sesana A., Lindfors E., Ramazani V. F., 2018, A&A, 615, A118

Sarkar A., Kushwaha P., Gupta A. C., Chitnis V. R., Wiita P. J., 2020, A&A, 642, A129

Sarkar A., Gupta A. C., Chitnis V. R., Wiita P. J., 2021, MNRAS, 501, 50

Scargle J. D., 1982, ApJ, 263, 835

Schlegel D. J., Finkbeiner D. P., Davis M., 1998, ApJ, 500, 525

Schulz M., Mudelsee M., 2002, Comput. Geosci., 28, 421

Shemmer O., Lieber S., 2015, ApJ, 805, 124

Shen Y. et al., 2019, ApJS, 241, 34

Shields J. C., 2007, in Ho L. C., Wang J. W., eds, ASP Conf. Ser. Vol. 373, The Central Engine of Active Galactic Nuclei. Astron. Soc. Pac., San Francisco, p. 355

Shukla A. et al., 2018, ApJ, 854, L26

Sillanpaa A., Haarala S., Valtonen M. J., Sundelius B., Byrd G. G., 1988, ApJ, 325, 628

Smith P. S., Montiel E., Rightley S., Turner J., Schmidt G. D., Jannuzi B. T., 2009, preprint (arXiv:0912.3621)

Sobacchi E., Sormani M. C., Stamerra A., 2017, MNRAS, 465, 161

Stella L., Vietri M., 1998, ApJ, 492, L59

Stickel M., Padovani P., Urry C. M., Fried J. W., Kuehr H., 1991, ApJ, 374, 431

Sun Q.-B. et al., 2023a, MNRAS, 518, 3901

Sun Q.-B., Qian S.-B., Zhu L.-Y., Liao W.-P., Zhao E.-G., Li F.-X., Shi X.-D., Li M.-Y., 2023b, MNRAS, 526, 3730

Sun Q.-B., Qian S.-B., Zhu L.-Y., Li Q.-M., Li F.-X., Li M.-Y., Li P., 2025, ApJ, 982, 127

Torrence C., Compo G. P., 1998, Bull. Am. Meteorol. Soc., 79, 61

Tripathi A., Gupta A. C., Aller M. F., Wiita P. J., Bambi C., Aller H., Gu M., 2021, MNRAS, 501, 5997

Ulrich M.-H., Maraschi L., Urry C. M., 1997, ARA&A, 35, 445

Urry C. M., Padovani P., 1995, PASP, 107, 803

Valtonen M., Karttunen H., 2006, The Three-Body Problem. Cambridge Univ. Press, Cambridge, UK

Valtonen M. J. et al., 2008, Nature, 452, 851

Vaughan S., 2005, A&A, 431, 391

Vaughan S., Edelson R., Warwick R. S., Uttley P., 2003, MNRAS, 345, 1271

Vaughan S., Uttley P., Markowitz A. G., Huppenkothen D., Middleton M. J., Alston W. N., Scargle J. D., Farr W. M., 2016, MNRAS, 461, 3145

Vestergaard M., Wilkes B. J., 2001, ApJS, 134, 1

Villata M., Raiteri C. M., 1999, A&A, 347, 30

Villforth C. et al., 2010, MNRAS, 402, 2087

White R. J., Peterson B. M., 1994, PASP, 106, 879

Wills B. J. et al., 1983, ApJ, 274, 62

Xiao H., Fan J., Ouyang Z., Hu L., Chen G., Fu L., Zhang S., 2022, ApJ, 936, 146

Xu Y., Bian W.-H., Yuan Q.-R., Huang K.-L., 2008, MNRAS, 389, 1703

Yip C. W. et al., 2004a, AJ, 128, 585

Yip C. W. et al., 2004b, AJ, 128, 2603

Zhang H., Wu F., Dai B., 2023, PASP, 135, 064102

Zhang H., Yan D., Zhang L., Tang N., 2025, MNRAS, 537, 2380

Zhang J., Zhang H.-M., Zhu Y.-K., Yi T.-F., Yao S., Lu R.-J., Liang E.-W., 2017, ApJ, 849, 42

Zhang P., Zhang P.-f., Yan J.-z., Fan Y.-z., Liu Q.-z., 2017, ApJ, 849, 9

Zhang P.-F., Yan D.-H., Zhou J.-N., Fan Y.-Z., Wang J.-C., Zhang L., 2017, ApJ, 845, 82

Zhang P.-f., Yan D.-h., Liao N.-h., Wang J.-c., 2017a, ApJ, 835, 260

Zhang P.-f., Yan D.-h., Liao N.-h., Zeng W., Wang J.-c., Cao L.-J., 2017b, ApJ, 842, 10

Zhang P.-f., Zhang P., Liao N.-h., Yan J.-z., Fan Y.-z., Liu Q.-z., 2018, ApJ, 853, 193

Zhang X. H., Bao G., 1991, A&A, 246, 21

Zheng W., Malkan M. A., 1993, ApJ, 415, 517

Zhou J., Wang Z., Chen L., Wiita P. J., Vadakkumthani J., Morrell N., Zhang P., Zhang J., 2018, Nat. Commun., 9, 4599

SUPPORTING INFORMATION

Supplementary data are available at *MNRAS* online.

suppl_data

Please note: Oxford University Press is not responsible for the content or functionality of any supporting materials supplied by the authors. Any queries (other than missing material) should be directed to the corresponding author for the article.

This paper has been typeset from a TeX/LaTeX file prepared by the author.